

Distribution of Eu²⁺ and Eu³⁺ Ions in Hydroxyapatite: A Cathodoluminescence and Raman Study

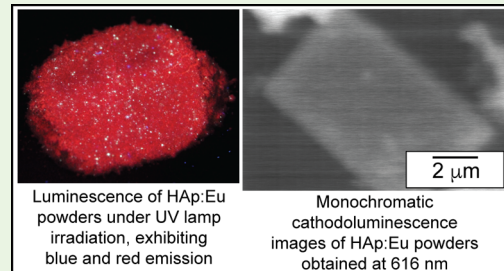
Luz A. Zavala-Sánchez,[†] Gustavo A. Hirata,[†] Ekaterina Novitskaya,[‡] Keyur Karandikar,[‡] Manuel Herrera,^{*,†} and Olivia A. Graeve^{*,†,‡}

[†]Centro de Nanociencias y Nanotecnología, Universidad Nacional Autónoma de México, Km 107 Carretera Tijuana-Ensenada, Ensenada, Baja California C.P. 22800, Mexico

[‡]Department of Mechanical and Aerospace Engineering, University of California, San Diego, 9500 Gilman Drive, MC 0411, La Jolla, California 92093-0411, United States

ABSTRACT: We present a cathodoluminescence study of the spatial distribution of Eu²⁺ and Eu³⁺ dopants in hydroxyapatite powders. The results demonstrate that the distribution of europium ions in the hydroxyapatite lattice depends on their valence state. Monochromatic cathodoluminescence images from prismatic powders show that although the Eu²⁺ is distributed homogeneously in the entire powder volume, the Eu³⁺ is present mainly at the powder edges. The luminescence spectrum of the Eu²⁺ ions displayed a wide and strong blue emission centered at 420 nm, while the luminescence spectrum of the Eu³⁺ ions displayed several orange-red emissions covering the range from 575 to 725 nm. These emissions correspond to transitions between levels 4f⁶5d¹-4f⁷ (⁸S_{7/2}) of the Eu²⁺ ions and ⁵D₀-⁷F_J levels of the Eu³⁺ ions. Micro Raman measurements reveal that europium doping generates two phonon signals with frequencies of 555 and 660 cm⁻¹, both of which have not been reported earlier. The powders were synthesized by the combustion synthesis method, maintaining constant the concentration of the europium salt used, and varying the pH of the precursor solutions to modify the concentration ratio of Eu²⁺ with respect to Eu³⁺. X-ray photoelectron spectroscopy measurements were used to determine values of 0.32 and 0.55 for the ratio Eu²⁺/Eu³⁺ in samples synthesized at pH values of 6 and 4, respectively. Thermal treatments of the samples, at 873 K in an oxygen atmosphere, resulted in a strong quenching of the Eu²⁺ luminescence due to oxidation of the Eu²⁺ ions into Eu³⁺, as well as probable elimination of calcium vacancy defects by annealing.

KEYWORDS: hydroxyapatite, europium, cathodoluminescence, monochromatic CL images



1. INTRODUCTION

Hydroxyapatite (Ca₁₀(PO₄)₆(OH)₂, HAp) is a material with potential applications as a drug and gene delivery agent,^{1,2} chromatographic adsorbent,³ gas sensor,⁴ and catalyst.^{5,6} Doped with rare-earth ions, this material can be used to acquire contrast-enhanced images from magnetic resonance, X-ray, and near-infrared reflection imaging,⁷ as well as applied as a fluorescent probe in medical technologies.^{8–11}

As one of the primary constituents of hard biological tissues, there is strong interest in this material mainly for applications in bone regeneration, as it shows great similarity with the mineral part of human bones.¹² HAp exhibits either monoclinic or hexagonal crystalline phases, with space groups P2₁/b and P6₃/m, respectively. The hexagonal phase can change to the monoclinic phase by heating at temperatures higher than 200 °C, due to displacements of the hydroxyl ions (OH⁻) in the crystal structure.¹³ The transformation between these two phases is poorly understood and reversibility has not been established. The unit cell of the hexagonal phase contains 44 atoms, with calcium ions showing two distinct stereochemistries, that is, Ca(I) with C₃ symmetry surrounded by nine oxygen atoms, and Ca(II) with C_s symmetry surrounded by six oxygen atoms and one (OH)⁻ ion. Furthermore, Ca(I)

and Ca(II) ions exhibit a relative abundance ratio of 4:6 and have low bond energy values that promote cationic exchange properties in the HAp lattice.^{9,14–16}

Considering its many uses, the preparation of HAp has received significant attention.^{17–19} For example, the material can be prepared by combustion synthesis in a single reaction step that allows the facile incorporation of rare-earth dopants into the structure. Specifically for europium doping, we have shown that the valence state of the europium ions is affected by calcium-deficiency in the structure.²⁰ The presence of only Eu³⁺ has been found in stoichiometric HAp, while a mixture of Eu³⁺ and Eu²⁺ has been detected in calcium-deficient HAp (Ca-D HAp). We previously reported that this effect can be explained by considering the destabilization of the Ca-D HAp:Eu crystal structure when Eu³⁺ ions substitute for Ca²⁺ ions, which require a charge compensation that forces the removal of a proton from the structure. We have postulated that the energy required to remove the protons from the Ca-D HAp:Eu structure might be too high, resulting in a significant amount of Eu²⁺ in the Ca²⁺

Received: September 2, 2015

Accepted: October 30, 2015

Published: October 30, 2015

sites of the crystal. Although other authors have reported the coexistence of Eu²⁺ and Eu³⁺ ions in different materials,^{21–24} there have been no reports on the distribution and quantification of these ions in HAp.

Cathodoluminescence (CL) is a highly effective technique to study the luminescent properties of various materials locally, providing spatial resolutions of several nanometers.²⁵ CL spectroscopy in the scanning electron microscope uses the electron beam as an excitation source, allowing one to obtain monochromatic and panchromatic CL images from different regions of a luminescent solid. In addition, this technique has the added advantage of operating at high excitation energy, allowing observation of optical transitions whose excitation is complicated or impossible to detect using conventional light sources.²⁶ CL is also considered a powerful technique to study the location and identification of crystal defects in semiconductors.^{27–29} It has also been used to investigate phosphorescent properties,^{30–32} radiation detector materials,³³ sedimentary rocks and petrographic marbles,^{34,35} and nanophosphor-assisted biological cell imaging.³⁶

In this work, we have used the CL technique to study the spatial distribution of Eu²⁺ and Eu³⁺ dopant ions in HAp:Eu. We have found that the valence state of the europium ion determines its position within the HAp:Eu microcrystals. While the Eu²⁺ is distributed homogeneously in the overall volume of the HAp powders, the Eu³⁺ is present mainly at the edges. In addition, XPS measurements reveal that the Eu²⁺/Eu³⁺ ratio changes as the pH is modified during synthesis of the powders.

2. EXPERIMENTAL PROCEDURE

Undoped and europium-doped hydroxyapatite samples were synthesized by combustion synthesis.^{37–43} An undoped sample [Ca₁₀(PO₄)₆(OH)₂, HAp] was prepared as a reference against the europium doped samples and is hereafter named HAp-ref. The reagents used were calcium nitrate tetrahydrate [Ca(NO₃)₂·4H₂O, 99%, Alfa Aesar, Ward Hill, MA], ammonium hydrogen phosphate [(NH₄)₂HPO₄, 98%, Alfa Aesar, Ward Hill, MA], and carbohydrazide [CO(NHNH₂)₂ 97%, Alfa Aesar, Ward Hill, MA]. Two europium-doped HAp samples, named HAp:Eu6 and HAp:Eu4 (the latter number referring to the pH of the solutions during synthesis) were prepared using europium nitrate hexahydrate [Eu(NO₃)₃·6H₂O, 99.9%, Alfa Aesar, Ward Hill, MA] as the dopant source.

The HAp-ref powders were prepared by dissolving 7.052 g of Ca(NO₃)₂·4H₂O into 29.86 mL of deionized water to form a 1.00 M solution and separately 2.366 g of (NH₄)₂HPO₄ were dissolved in 26.87 mL of deionized water to form a 0.67 M solution. The (NH₄)₂HPO₄ solution was then added dropwise to the Ca(NO₃)₂·4H₂O solution under continuous stirring, maintaining a ratio of Ca to P of 1.67, which is the stoichiometric ratio in HAp. The native pH value of this solution was approximately 6. Subsequently, 4.035 g of carbohydrazide were dissolved into the mixed solution and placed in a Pyrex crystallization dish, to be introduced into a furnace preheated at 773 K until ignition occurred (within approximately 7 min).

The HAp:Eu6 and HAp:Eu4 powders were prepared by dissolving separately 6.346 g of Ca(NO₃)₂·4H₂O and 0.656 g of Eu(NO₃)₃·6H₂O in 28.28 mL of deionized water to form a 1.00 M solution, and 2.2412 g of (NH₄)₂HPO₄ in 25.45 mL of deionized water to form a 0.67 M solution. This followed the same mixing procedure and carbohydrazide incorporation as in the HAp-ref synthesis. For the HAp:Eu4 powders, the pH of the Ca(NO₃)₂·4H₂O/Eu(NO₃)₃·6H₂O solution was adjusted to 4 using a 1.00 M HNO₃ solution. After synthesis, the samples were calcined at 873 K in a tube furnace using an O₂ (99.99%) flow rate of 4 mL/min for 4 h.

As-synthesized and calcined samples were characterized with a Bruker D2 Phaser X-ray diffractometer, using CuK α radiation and a step size of 0.01° over the 2θ range of 20 to 80 degrees. Raman

spectroscopy was completed on a Horiba Jobin-Yvon LabRam HR800 confocal microscope with a 630 nm laser at 300 K. Particle size distributions were determined using a Microtrac Nanotrac ULTRA dynamic light scattering (DLS) system,^{44–56} dispersing approximately 0.48 g of powder in 25 mL of ethanol, stirring for 15 min and ultrasonicating for 5 min. Energy-dispersive spectroscopy was used to determine elemental composition using an X-Max Oxford-Instruments system with a detector size of 20 mm². The morphology of the powders was evaluated by scanning electron microscopy (SEM) using a JEOL JIB-4500 instrument and transmission electron microscopy (TEM) using a JEOL JEM-2010 instrument operated at 200 kV. CL measurements were performed in the SEM using a Gatan MonoCL4 system at 300 K in the UV-visible spectral range. Monochromated images of the Eu²⁺ and Eu³⁺ emissions were obtained by fixing the diffraction grating at wavelengths of 425 and 615 nm, respectively. X-ray photoelectron spectroscopy (XPS) measurements were acquired in a SPECS system equipped with a PHOIBOS WAL analyzer using an Al anode. XPS measurements were performed after a sputtering treatment with Ar⁺ ions at 3 keV for 15 s, using an energy pass of 5 eV. High-resolution spectra were obtained using 300 scans during the measurement, using windows of 0.1 eV sensitivity. To estimate the areal intensity of Eu³⁺ and Eu²⁺ components, we deconvoluted final spectra into Gaussian peaks using a Shirley background with the aid of CasaXPS processing software. Hydra-Medusa software was used to obtain the chemical equilibrium diagram of Eu species at different pH values, considering the Eu concentration of the prepared powders.⁵⁷

3. RESULTS AND DISCUSSION

3.1. General Powder Characteristics. From XRD analysis (Figure 1), the as-synthesized and calcined samples consist

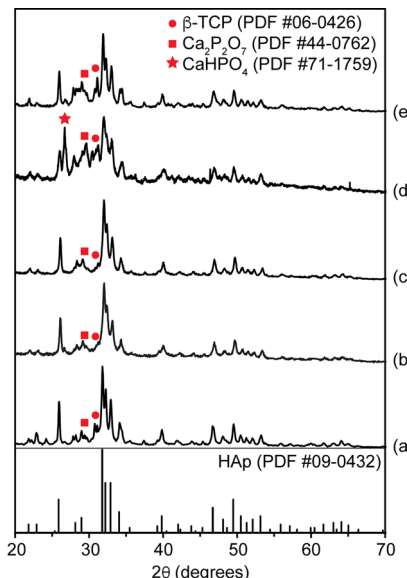


Figure 1. X-ray diffraction of the HAp and HAp:Eu samples: (a) HAp-ref, (b) as-synthesized HAp:Eu6, (c) calcined HAp:Eu6, (d) as-synthesized HAp:Eu4, and (e) calcined HAp:Eu4.

of hexagonal hydroxyapatite with lattice parameters $a = b = 0.9446$ nm and $c = 0.6890$ nm for the HAp-ref, $a = b = 0.9480$ nm and $c = 0.6829$ nm for the HAp:Eu6 powders, and $a = b = 0.9433$ nm and $c = 0.6858$ nm for the HAp:Eu4 powders. These lattice parameter values are essentially the same as those reported in PDF card #09–0432. The formation of calcium deficient hydroxyapatite (Ca-D HAp) phase in these samples cannot be ruled out since this phase shows overlapping diffraction peaks with the hexagonal hydroxyapatite phase. XRD patterns from the doped as-synthesized and calcined powders

also show a peak at about 29 degrees 2θ that corresponds to a residual calcium pyrophosphate ($\text{Ca}_2\text{P}_2\text{O}_7$) phase. Similarly, peaks associated with residual β -tricalcium phosphate (β -TCP) and CaHPO_4 appear in the powders. For both doped samples no europium oxide phases were found before or after calcination. The atomic compositions of the samples from energy dispersive spectroscopy are listed in **Table 1**, revealing about 1 at % of

Table 1. Atomic Composition of the As-Synthesized and Calcined Samples from Energy-Dispersive Spectroscopy Measurements

	pH	Ca (at %)	P (at %)	Eu (at %)	O (at %)	Ca/P ratio
HAp-ref	6	22.5	13.5	0.0	64.1	1.66
HAp:Eu6 (as-synthesized)	6	18.5	12.3	1.4	67.8	1.62
HAp:Eu6 (calcined)	6	19.0	12.3	1.4	67.4	1.65
HAp:Eu4 (as-synthesized)	4	17.7	12.3	1.2	68.8	1.54
HAp:Eu4 (calcined)	4	17.6	11.6	1.2	69.7	1.61

europerium for both doped samples. For the HAp-ref and HAp:Eu6 samples, the calculated $(\text{Ca}+\text{Eu})/\text{P}$ atomic ratio values were near stoichiometric HAp (1.66). The ratio was lower for the as-synthesized and calcined HAp:Eu4 powders, suggesting the formation of a larger amount of Ca-D HAp in this particular sample.

The effect of pH on the combustion synthesis of Ca-D HAp is illustrated in **Figure 2**. Starting from solutions of Ca^{2+} , Eu^{3+}

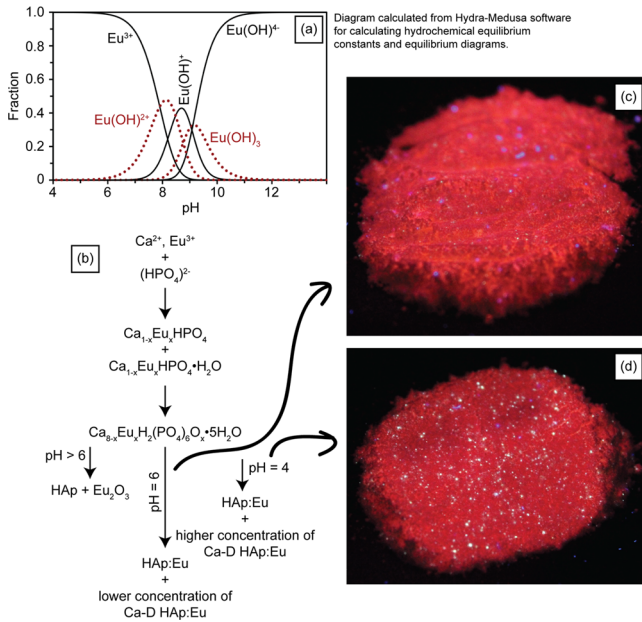


Figure 2. (a) Formation mechanism of Eu^{2+} in HAp and Ca-D HAp samples and speciation diagram of Eu simulated with Hydra-Medusa software. Luminescence images of the samples for (b) HAp:Eu6 and (c) HAp:Eu 4, generated by UV irradiation revealing the emission of red and blue light, respectively.

and $(\text{HPO}_4)^{2-}$ ions (**Figure 2b**), the formation of soluble calcium orthophosphates, CaHPO_4 (monetite) and $\text{CaHPO}_4 \cdot \text{H}_2\text{O}$ (brushite), is first observed. During exposure to the high

temperatures provided by the exothermicity of the combustion reaction, these phases nucleate into the intermediate compound $\text{Ca}_{8-x}\text{Eu}_x\text{H}_2(\text{PO}_4)_6 \cdot 5\text{H}_2\text{O}$ (OCP).⁵⁸ Under alkaline pH, this compound can become HAp.⁵⁹ The speciation diagram calculated for a concentration of Eu^{3+} of 0.05 M in the precursor solution (**Figure 2a**) shows that at pH > 6 the Eu^{3+} transforms into $\text{Eu}(\text{OH})^{2+}$ and $\text{Eu}(\text{OH})^+$, possibly increasing the probability of the formation of Eu_2O_3 . Diaz de Leon et al.⁶⁰ have reported similar diagrams for other systems. At the unmodified pH of the precursor solution (pH 6) the intermediate compound OCP becomes mostly HAp with a small amount of the Ca-D HAp phase. Under acidic conditions (pH = 4), the OCP compound hydrolyzes to form HAp crystals with a larger amount of CaD-HAp, as a result of the limited OH^- concentration in the solution. The formation of the CaD-HAp phase then results in the generation of a high Eu^{2+} concentration, which emits in the blue part of the electromagnetic spectrum. One can see from **Figure 2c, d** that the HAp:Eu4 sample emits more strongly in the blue compared to the HAp:Eu6 sample. As has been described previously,²⁰ the substitution of Eu^{3+} ions for Ca^{2+} in the Ca-D HAp lattice requires charge compensation that forces the reduction of Eu^{3+} to Eu^{2+} .

The XPS spectrum of the calcined HAp:Eu6 powders with O 1s, Ca 2p_{3/2}, and P 2p signals centered at binding energies of 531.0, 347.2, and 133.1 eV, respectively, is illustrated in **Figure 3a**. The signal for Eu 3d_{5/2} is also marked in the figure and will be discussed later. Similar XPS spectra were obtained

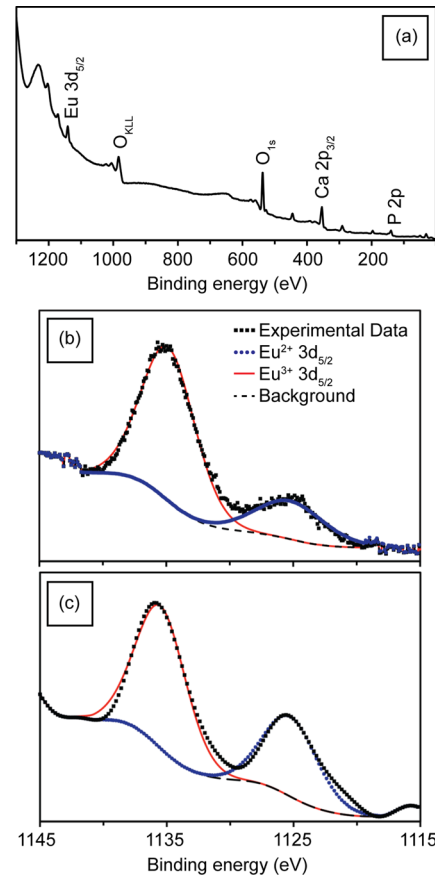


Figure 3. (a) X-ray photoelectron spectrum (XPS) of the calcined samples with signals of Eu (3d), O (1s), Ca (2p), and P (2p). (b) XPS signals of Eu^{2+} and Eu^{3+} of the calcined HAp:Eu6. (c) XPS signals of the Eu^{2+} and Eu^{3+} of the calcined HAp:Eu4.

for the HAp-ref and HAp:Eu4 powders (not shown), with the same experimental outcomes, except that the HAp-ref powders obviously did not contain a europium signal. The Eu $3d_{5/2}$ signals are centered at 1125.6 and 1135.3 eV for the calcined HAp:Eu6 (Figure 3b) and HAp:Eu4 (Figure 3c) samples. These signals correspond to europium oxidation states of +2 and +3, respectively,^{61,62} and reveal different relative intensities for each sample. Table 2 lists values of the concentrations of

Table 2. Concentration Ratio $\text{Eu}^{2+}/\text{Eu}^{3+}$ in the Doped HAp Samples after Calcination, Determined from X-ray Photoelectron Spectroscopy Measurements

	ion	binding energy $3d_{5/2}$ (eV)	partial concentration (at %)	$\text{Eu}^{2+}/\text{Eu}^{3+}$ ratio
HAp:Eu6 (calcined)	Eu^{2+}	1135.3	24.0	0.3
	Eu^{3+}	1125.6	76.0	
HAp:Eu4 (calcined)	Eu^{2+}	1135.3	35.0	0.5
	Eu^{3+}	1125.6	65.0	

europium and the $\text{Eu}^{2+}/\text{Eu}^{3+}$ ratio, calculated from the area ratio of the two XPS deconvoluted curves. These results show a higher surface concentration of Eu^{2+} in the HAp:Eu4 powders than in the HAp:Eu6 powders, a trend that can be explained based on the arguments presented previously and outlined in Figure 2. Therefore, we conclude that the rise of Eu^{2+} concentration shown in our XPS results for the HAp:Eu4 is related to an increase in Ca-D HAp. This is also supported by our XRD results.

SEM images of the HAp:Eu6 powders show formation of nanoparticles irregularly agglomerated (Figure 4a), with average

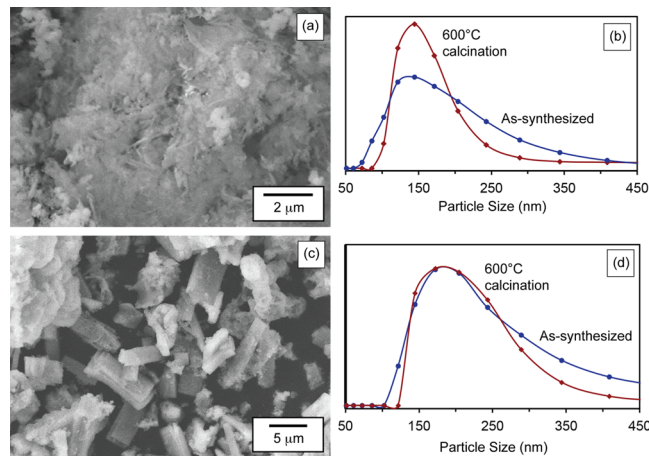


Figure 4. Scanning electron micrographs of (a) HAp:Eu6 and (c) HAp:Eu4. The corresponding DLS histograms are illustrated in b and d, respectively.

hard agglomerate diameters between 150 and 167 nm as revealed by DLS measurements (Figure 4b). SEM images of HAp:Eu4 calcined powders show the formation of numerous prismatic HAp microcrystals with lengths between 2 and 7 μm , and widths lower than 5 μm (Figure 4c). These powders also contain smaller agglomerates of average diameter between 160 and 170 nm, as determined from DLS measurements (Figure 4d). Although geometric CaP crystals have been previously synthesized by the hydrothermal method at pH 4, the thermodynamic conditions of this method promote the formation of other undesired calcium phosphate phases that

become dominant, such as CaHPO_4 , $\text{CaHPO}_4 \cdot 2\text{H}_2\text{O}$, and $\text{Ca}_8(\text{HPO}_4)_2(\text{PO}_4)_4 \cdot \text{OH}_2$,¹⁷ an outcome not observed in our HAp:Eu4 powders. From TEM (Figure 5), we also see nanorods

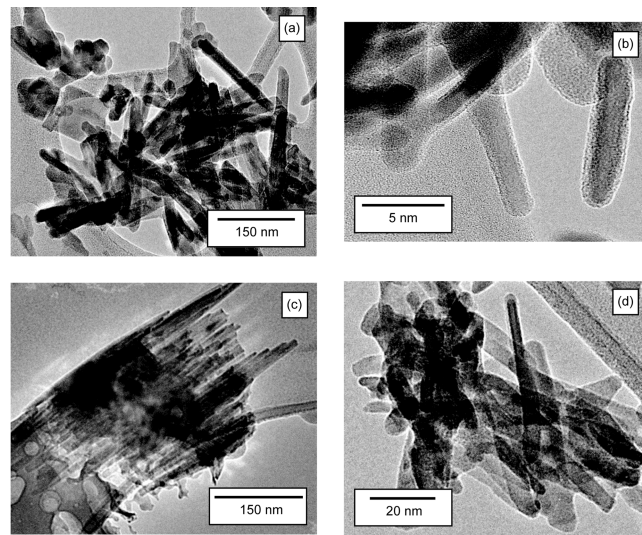


Figure 5. Transmission electron micrographs of the calcined (a, b) HAp:Eu6 and (c, d) HAp:Eu4 powders.

of several hundreds of nanometers in length and widths lower than 5 nm for the HAp:Eu6 powders (Figure 5a, b) and prismatic microstructures of about 10 nm in diameter for the HAp:Eu4 powders (Figure 5c, d).

2.2. Effects of Europium on the Luminescence and Vibration Responses of HAp.

The influence of the europium ions in the hydroxyapatite host were evaluated by micro-Raman spectroscopy (Figure 6). The Raman spectrum of the HAp-ref

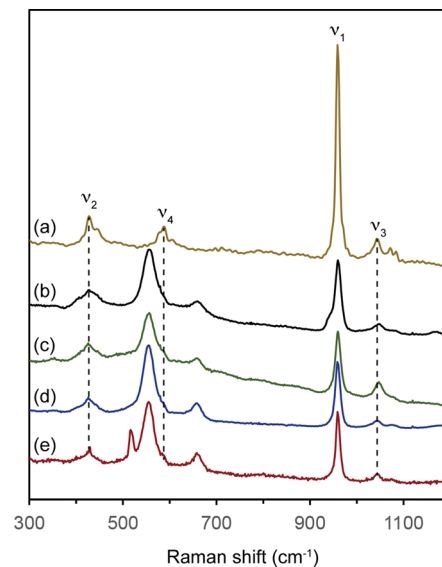


Figure 6. Raman spectra of (a) HAp-ref, (b) as-synthesized HAp:Eu6, (c) calcined HAp:Eu6, (d) as-synthesized HAp:Eu4, and (e) calcined HAp:Eu4 calcined.

powders (Figure 6a) reveals four peaks centered at 428, 580, 960, and 1043 cm^{-1} , which correspond to the ν_2 , ν_4 , ν_1 , and ν_3 vibrational modes of the phosphate ions, respectively.^{63,64} The Raman spectra of the as-synthesized and calcined doped samples (Figure 6b, e) show the same phonon signals, although

clearly attenuated in intensity as an effect of the europium incorporation in the HAp host.^{65,66} The spectra of the europium doped samples also show the presence of two signals centered at 555 and 660 cm⁻¹, apparently generated by vibrational modes of the phosphate ions bonded to the europium ions. These are Raman signals that, to the best of our knowledge, have never been seen before in HAp, though are present in other phosphate compounds. De Aza et al.⁶⁷ have reported a Raman signal centered at 555 cm⁻¹ in polycrystalline β -TCP, generated by the ν_4 vibrational mode of the phosphate ions. Similarly, Koudelka and Mosner⁶⁸ have reported a signal centered at 660 cm⁻¹ in boron phosphate samples, attributing their origin to symmetric stretching vibrations of the phosphate ions bonded to the boron atoms. CL spectra (Figure 7) of the samples show a broad

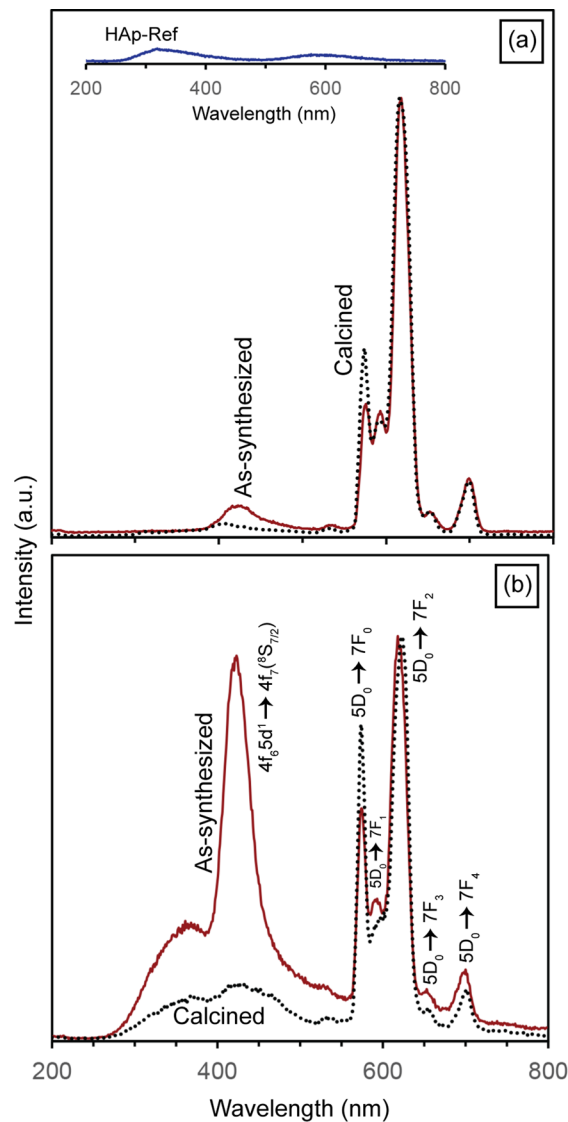


Figure 7. (a) Cathodoluminescence spectra of as-synthesized HAp-ref, as-synthesized HAp:Eu6 and calcined HAp:Eu6. (b) Cathodoluminescence spectra of the as-synthesized and calcined HAp:Eu4.

UV-blue emission in the range between 300 and 475 nm, and several orange-red bands between 575 and 725 nm. The UV-blue emission corresponds to transitions between levels $4f^6 5d^1$ and $4f^7 ({}^8S_{7/2})$ of the Eu²⁺ ions,⁶⁹ whereas the orange-red emission corresponds to the transitions between $5D_0$ and

$7F_j$ of the Eu³⁺ ions. Moreover, CL spectra show that the as-synthesized HAp:Eu4 powders (Figure 7a) exhibit a strong Eu²⁺ emission, which we explain as a result of the formation of the Ca-D HAp:Eu phase. Table 1 shows that the atomic ratio Ca/P of the HAp:Eu4 sample is clearly lower than the expected value for stoichiometric HAp (1.67), revealing calcium deficiency in the sample. As described earlier, we have found the presence of significant amounts of Eu²⁺ in Ca-D HAp:Eu that was explained in terms of destabilization of the crystal structure when Eu³⁺ ions substitute for Ca²⁺ ions.²⁰ On the other hand, Zahn and Hochrein⁷⁰ have reported that Ca-D HAp show a preference for Ca²⁺ vacancy defects (V_{Ca}^{2+}) accompanied by charge neutralization by adjacent H₂O and HPO₄²⁻ defects. Moreover, Sun et al.⁷¹ recently reported that V_{Ca}^{2+} defects are the most stable defect in HAp, with a formation energy of only 0.39 eV. Because the HAp:Eu4 sample showed a strong Eu²⁺ emission, we conclude that adjusting of pH to 4 during synthesis induces the formation of Ca-D HAp phase as well as V_{Ca}^{2+} point defects. In Figure 7b, we also see a strong decrease in the relative intensity of the Eu²⁺ emission after the calcination treatment, which can be attributed to the oxidation of Eu²⁺ to Eu³⁺ and possibly by the annealing of the V_{Ca}^{2+} defects.⁷²

Whereas panchromatic CL images of the as-synthesized HAp:Eu6 powders show a homogeneous luminescence (Figure 8a, b), corresponding to a uniform distribution of Eu³⁺,

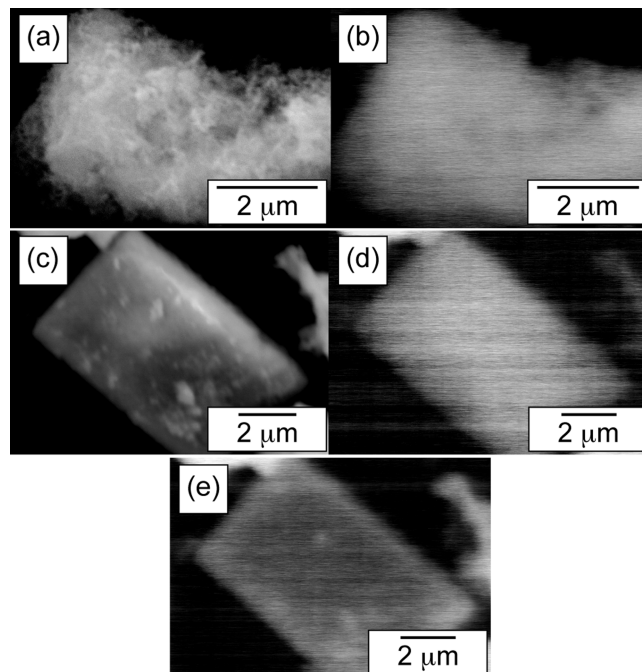


Figure 8. (a) Secondary electron and (b) panchromatic cathodoluminescence images of HAp:Eu6. (c) Secondary and monochromatic cathodoluminescence images of HAp:Eu4 obtained at (d) 425 and (e) 616 nm.

monochromatic CL images of the as-synthesized HAp:Eu4 powders show an inhomogeneous spatial distribution of the Eu²⁺ and Eu³⁺ emissions (Figure 8c, d). Monochromatic CL images obtained at a fixed wavelength of 425 nm (Figure 8d) to analyze the Eu²⁺ emission, show homogeneous intensity throughout the microcrystals, whereas monochromatic CL images acquired at a fixed wavelength of 616 nm (Figure 8e) to analyze the Eu³⁺ stronger emission, show brighter regions at the edges of the microcrystals. This contrast could be ascribed

to a higher CL emission associated with the higher specific free surface of the microcrystals at the edges. However, since this effect is not observed in the CL images obtained at 425 nm (Figure 8d), the CL image obtained at 616 nm represents mainly the Eu³⁺ distribution. Thus, Eu²⁺ ions are present in the entire volume of the HAp particles, whereas the Eu³⁺ ions are present mainly at the edges. We attribute this effect to the strong stability of the V_{Ca}²⁺ defects in the entire volume of the Ca-D HAp lattice,⁶⁹ whose formation correlates with the presence of Eu²⁺ ions in the HAp:Eu4 sample.

In summary, we report a cathodoluminescence study demonstrating the segregation of europium ions in doped HAp. The Eu²⁺ ions are present in the entire volume of the HAp particles, whereas the Eu³⁺ ions are present mainly at the edges. Micro-Raman measurements confirmed the incorporation of europium in HAp, revealing two phonon signals with frequencies of 555 and 660 cm⁻¹.

4. CONCLUSIONS

Undoped and europium-doped hydroxyapatite powders were synthesized by combustion synthesis controlling the pH of the Ca/Eu precursor solution. Two europium-doped samples were grown at pH values of 6 (HAp:Eu6) and 4 (HAp:Eu4), revealing a morphology of nanopowders and prismatic microstructures, respectively. The presence of Eu²⁺ and Eu³⁺ in the powders was confirmed by XPS measurements, revealing a surface concentration ratio Eu²⁺/Eu³⁺ of about 0.32 and 0.55 for samples HAp:Eu6 and HAp:Eu4, respectively. Cathodoluminescence (CL) spectra revealed the formation of a broad UV-blue emission in the 300 and 475 nm range and several orange-red bands between 575 and 725 nm, attributed to the Eu²⁺ and Eu³⁺ emissions, respectively. Monochromatic CL images of the powders grown at pH 4 exhibited an inhomogeneous spatial distribution of the Eu²⁺ and Eu³⁺ emissions. The Eu²⁺ emission was generated homogeneously in the HAp:Eu4 prismatic microstructures while the Eu³⁺ emission was generated at the edges and surfaces. These results show that Eu²⁺ and calcium vacancies (V_{Ca}) are present in all the volume of the prismatic HAp microstructures, whereas Eu³⁺ is predominantly present at the edges and lateral faces. A thermal treatment at 873 K in O₂ atmosphere revealed a strong quenching of the Eu²⁺ CL emission, due to both the oxidation of Eu²⁺ ions and the elimination of V_{Ca} defects.

AUTHOR INFORMATION

Corresponding Authors

*E-mail: zaldivar@cnyn.unam.mx.

*E-mail: ograeve@ucsd.edu. Tel: (858) 246-0146. URL: <http://ograeve.ucsd.edu/>.

Notes

The authors declare no competing financial interest.

ACKNOWLEDGMENTS

This work was supported by a grant from the National Science Foundation (1334160) and a grant from PAPIIT-UNAM (IN104414). The technical assistance of J.N. Díaz de León, I. Pérez-Montfort, and J. Díaz is greatly appreciated.

REFERENCES

- (1) Itokazu, M.; Yang, W.; Aoki, T.; Ohara, A.; Kato, N. Synthesis of antibiotic-loaded interporous hydroxyapatite blocks by vacuum method and in vitro drug release testing. *Biomaterials* **1998**, *19*, 817–819.
- (2) Lee, L.; Upadhye, K.; Kumta, P. N. Nano-sized calcium phosphate (CaP) carriers for non-viral gene delivery. *Mater. Sci. Eng., B* **2012**, *177*, 289–302.
- (3) Cummings, L. J.; Snyder, M. A.; Brisack, K. Protein chromatography on hydroxyapatite columns. *Methods Enzymol.* **2009**, *463*, 387–404.
- (4) Mene, R. U.; Mahabole, M. P.; Khairnar, R. S. Surface modified hydroxyapatite thick films for CO₂ gas sensing application: Effect of swift heavy ion irradiation. *Radiat. Phys. Chem.* **2011**, *80*, 682–687.
- (5) Vukomanovic, M.; Zunic, V.; Otonicar, M.; Repnik, U.; Turk, B.; Skapin, S. D.; Suvorov, D. Hydroxyapatite/platinum bio-photocatalyst: a biomaterial approach to self-cleaning. *J. Mater. Chem.* **2012**, *22*, 10571–10580.
- (6) Anmin, H.; Tong, L.; Ming, L.; Chengkang, C.; Huiqin, L.; Dali, M. Preparation of nanocrystals hydroxyapatite/TiO₂ compound by hydrothermal treatment. *Appl. Catal., B* **2006**, *63*, 41–44.
- (7) Ashokan, A.; Menon, D.; Nair, S.; Koyakutty, M. A molecular receptor targeted, hydroxyapatite nanocrystal based multi-modal contrast agent. *Biomaterials* **2010**, *31*, 2606–2616.
- (8) De Araujo, T. S.; Macedo, Z. S.; De Oliveira, P. A. S. C.; Valerio, M. E. G. Production and characterization of pure and Cr³⁺-doped hydroxyapatite for biomedical applications as fluorescent probes. *J. Mater. Sci.* **2007**, *42*, 2236–2243.
- (9) Jagannathan, R.; Kottaisamy, M. Eu³⁺ luminescence: a spectral probe in M₅(PO₄)₃X apatites (M = Ca or Sr; X = F⁻, Cl⁻, Br⁻ or OH⁻). *J. Phys.: Condens. Matter* **1995**, *7*, 8453–8466.
- (10) Li, L.; Liu, Y.; Tao, J.; Zhang, M.; Pan, H.; Xu, X. Surface modification of hydroxyapatite nanocrystallite by a small amount of terbium provides a biocompatible fluorescent probe. *J. Phys. Chem. C* **2008**, *112*, 12219–12224.
- (11) Pappalardo, R. G.; Walsh, J.; Hunt, R. B. Cerium-activated halophosphate phosphors. *J. Electrochem. Soc.* **1983**, *130*, 2087–2096.
- (12) Malmberg, P.; Nygren, H. Methods for the analysis of the composition of bone tissue, with a focus on imaging mass spectrometry (TOF-SIMS). *Proteomics* **2008**, *8*, 3755–3762.
- (13) Elliott, J. C. In *Structure and Chemistry of the Apatites and Other Calcium Orthophosphates*; Academic Press, Waltham, MA, 1994.
- (14) Tsukada, M.; Wakamura, M.; Yoshida, N.; Watanabe, T. Band gap and photocatalytic properties of Ti-substituted hydroxyapatite: comparison with anatase-TiO₂. *J. Mol. Catal. A: Chem.* **2011**, *338*, 18–23.
- (15) Suzuki, T.; Hatushika, T.; Hayakawa, Y. Synthetic hydroxyapatites employed as inorganic cation-exchangers. *J. Chem. Soc., Faraday Trans. 1* **1981**, *77*, 1059–1062.
- (16) Zhenping, Q.; Yahui, S.; Chen, D.; Wang, Y. Possible sites of copper located on hydroxyapatite structure and the identification of active sites for formaldehyde oxidation. *J. Mol. Catal. A: Chem.* **2014**, *393*, 182–190.
- (17) Sadat-Shojaei, M.; Khorasani, M.-T.; Dinpanah-Khoshdargi, E.; Jamshidi, A. Synthesis methods for nanosized hydroxyapatite with diverse structures. *Acta Biomater.* **2013**, *9*, 7591–7621.
- (18) Koutsopoulos, S. Synthesis and characterization of hydroxyapatite crystals: a review study on the analytical methods. *J. Biomed. Mater. Res.* **2002**, *62*, 600–612.
- (19) Vallet-Regí, M.; González-Calbet, J. M. Calcium phosphates as substitution of bone tissues. *Prog. Solid State Chem.* **2004**, *32*, 1–31.
- (20) Graeve, O. A.; Kanakala, R.; Madadi, A.; Williams, B. C.; Glass, K. C. Luminescence variations in hydroxyapatites doped with Eu²⁺ and Eu³⁺. *Biomaterials* **2010**, *31*, 4259–4267.
- (21) Dai, W. B. Mechanism of the reduction and energy transfer between Eu²⁺ and Eu³⁺ in Eu-doped CaAl₂Si₂O₈ materials prepared in air. *J. Mater. Chem. C* **2014**, *2*, 3951–3959.
- (22) Zhang, J. C.; Long, Y. Z.; Zhang, H. D.; Sun, B.; Han, W. P.; Sun, X. Y. Eu²⁺/Eu³⁺-emission-ratio-tunable CaZr(PO₄)₂:Eu phosphors synthesized in air atmosphere for potential white light-emitting deep UV LEDs. *J. Mater. Chem. C* **2014**, *2*, 312.
- (23) Panatarani, C.; Lenggoro, I. W.; Okuyama, K. The crystallinity and the photoluminescent properties of spray pyrolyzed ZnO

- phosphor containing Eu⁺² and Eu⁺³ ions. *J. Phys. Chem. Solids* **2004**, *65*, 1843–1847.
- (24) Chen, X.; Zhao, J.; Yu, L.; Rong, C.; Li, C.; Lian, S. A. White light emitting phosphor Sr_{1.5}Ca_{0.5}SiO₄:Eu³⁺, Tb³⁺, Eu²⁺ for LED-based near-UV chip: Preparation, characterization and luminescent mechanism. *J. Lumin.* **2011**, *131*, 2697–2702.
- (25) Poelman, D.; Smet, P. F. Time resolved microscopic cathodoluminescence spectroscopy for phosphor research. *Phys. B* **2014**, *439*, 35–40.
- (26) Trofimov, A. N.; Zamoryanskaya, M. V. Characterization of radiative centers in wide-band-gap materials by local cathodoluminescence by the example of europium-doped YAG. *J. Surf. Invest.: X-Ray, Synchrotron Neutron Tech.* **2009**, *3*, 15–20.
- (27) Zamoryanskaya, M. V.; Domracheva, Y. V.; Shakhmin, A. A.; Shustov, D. B.; Trofimov, A. N.; Konnikov, S. G. Local cathodoluminescence study of defects in semiconductors and multilayer structures. *Phys. B* **2009**, *404*, 5042–5044.
- (28) González, A.; Herrera, M.; Valenzuela, J.; Escobedo, A.; Pal, U. Cathodoluminescence evaluation of defect structures in hydrothermally grown ZnO:Sb nanorods. *J. Nanosci. Nanotechnol.* **2011**, *11*, 5526–5531.
- (29) Guzmán, G.; Herrera, M.; Valenzuela, J.; Maestre, D. CL study of blue and UV emissions in β-Ga₂O₃ nanowires grown by thermal evaporation of GaN. *J. Appl. Phys.* **2011**, *110*, 034315.
- (30) Ramakrishna, P. V. Cathodoluminescence properties of gadolinium-doped CaMoO₄:Eu nanoparticles. *Spectrochim. Acta, Part A* **2015**, *149*, 312–316.
- (31) Ekdal, E.; Garcia, J.; Kelemen, A.; Ayvacikli, M.; Canimoglu, A.; Jorge, A.; Karali, T.; Can, N. Cathodoluminescence and Raman characteristics of CaSO₄:Tm³⁺, Cu phosphor. *J. Lumin.* **2015**, *161*, 358–362.
- (32) Tomala, R.; Marciniak, L.; Jiang, L.; Yubai, P.; Lenczewska, K.; Strek, W.; Hreniak, D. A comprehensive study of photoluminescence and cathodoluminescence of YAG:Eu³⁺ nano- and microceramics. *Opt. Mater.* **2015**, DOI: [10.1016/j.optmat.2015.06.042](https://doi.org/10.1016/j.optmat.2015.06.042).
- (33) Tyrrell, G. C. Phosphors and scintillators in radiation imaging detectors. *Nucl. Instrum. Methods Phys. Res., Sect. A* **2005**, *546*, 180–187.
- (34) Omer, M. F. Cathodoluminescence petrography for provenance studies of the sandstones of Ora formation (Devonian–Carboniferous), Iraqi Kurdistan region, northern Iraq. *J. Afr. Earth Sci.* **2015**, *109*, 195–210.
- (35) Jarc, S.; Zupancic, N. A. Cathodoluminescence and petrographical study of marbles from the Pohorje area in Slovenia. *Chem. Erde* **2009**, *69*, 75–80.
- (36) Niioka, H.; Furukawa, T.; Ichimiya, M.; Ashida, M.; Araki, T.; Hashimoto, M. Multicolor cathodoluminescence microscopy for biological imaging with nanophosphors. *Appl. Phys. Express* **2011**, *4*, 112402.
- (37) Lopez, O. A.; McKittrick, J. M.; Shea, L. E. Fluorescence properties of polycrystalline Tm³⁺ activated Y₃Al₅O₁₂ and Tm³⁺-Li⁺ co-activated Y₃Al₅O₁₂ in the visible and near IR Ranges. *J. Lumin.* **1997**, *71*, 1–11.
- (38) Shea, L. E.; McKittrick, J.; Lopez, O. A.; Sluzky, E.; Phillips, M. L. F. Advantages of self-propagating combustion reactions for synthesis of oxide phosphors. *J. Soc. Inf. Disp.* **1997**, *5*, 117–125.
- (39) Shea, L. E.; McKittrick, J.; Lopez, O. A.; Sluzky, E. Synthesis of red-emitting, small particle size oxide phosphors using an optimized combustion process. *J. Am. Ceram. Soc.* **1996**, *79*, 3257–3265.
- (40) Shea, L. E.; McKittrick, J.; Lopez, O. A.; Sluzky, E. Effect of processing parameters on luminescence of combustion-synthesized, rare earth activated Y₃Al₅O₁₂ phosphors. *Ceram. Trans.* **1996**, *67*, 105–108.
- (41) Kanakala, R.; Escudero, R.; Rojas-George, G.; Ramisetty, M.; Graeve, O. A. Mechanisms of combustion synthesis and magnetic response of high-surface-area hexaboride compounds. *ACS Appl. Mater. Interfaces* **2011**, *3*, 1093–1100.
- (42) Kanakala, R.; Rojas-George, G.; Graeve, O. A. Unique preparation of hexaboride nanocubes: A first example of boride formation by combustion synthesis. *J. Am. Ceram. Soc.* **2010**, *93*, 3136–3141.
- (43) Graeve, O. A.; Varma, S.; Rojas-George, G.; Brown, D.; Lopez, E. A. Synthesis and characterization of luminescent yttrium oxide doped with Tm and Yb. *J. Am. Ceram. Soc.* **2006**, *89*, 926–931.
- (44) Cahill, J. T.; Ruppert, J. N.; Wallis, B.; Liu, Y.; Graeve, O. A. Development of mesoporosity in scandia-stabilized zirconia: particle size, solvent, and calcination effects. *Langmuir* **2014**, *30*, 5585–5591.
- (45) Vargas-Consuelos, C. I.; Seo, K.; Camacho-Lopez, M.; Graeve, O. A. Correlation between particle size and Raman vibrations in WO₃ Powders. *J. Phys. Chem. C* **2014**, *118*, 9531–9537.
- (46) Graeve, O. A.; Fathi, H.; Kelly, J. P.; Saterlie, M. S.; Sinha, K.; Rojas-George, G.; Kanakala, R.; Brown, D. R.; Lopez, E. A. Reverse micelle synthesis of oxide nanopowders: mechanisms of precipitate formation and agglomeration effects. *J. Colloid Interface Sci.* **2013**, *407*, 302–309.
- (47) Higgins, B.; Graeve, O. A.; Edwards, D. D. New methods for preparing submicron powders of the tungstate-ion conductor Sc₂(WO₄)₃ and its Al and In analogs. *J. Am. Ceram. Soc.* **2013**, *96*, 2402–2410.
- (48) Saterlie, M. S.; Sahin, H.; Kavlicoglu, B.; Liu, Y.; Graeve, O. A. Surfactant effects on dispersion characteristics of copper-based nanofluids: A dynamic light scattering study. *Chem. Mater.* **2012**, *24*, 3299–3306.
- (49) Fathi, H.; Kelly, J. P.; Vasquez, V. R.; Graeve, O. A. Ionic concentration effects on reverse micelle size and stability: Implications for the synthesis of nanoparticles. *Langmuir* **2012**, *28*, 9267–9274.
- (50) Saterlie, M. S.; Sahin, H.; Kavlicoglu, B.; Liu, Y.; Graeve, O. A. Particle size effects in the thermal conductivity enhancement of copper-based nanofluids. *Nanoscale Res. Lett.* **2011**, *6*, 217.
- (51) Kelly, J. P.; Graeve, O. A. Statistical experimental design approach for the solvothermal synthesis of nanostructured tantalum carbide powders. *J. Am. Ceram. Soc.* **2011**, *94*, 1706–1715.
- (52) Vasquez, V. R.; Williams, B. C.; Graeve, O. A. Stability and comparative analysis of AOT/Water/Isooctane reverse micelles system using dynamic light scattering and molecular dynamics. *J. Phys. Chem. B* **2011**, *115*, 2979–2987.
- (53) Kelly, J. P.; Kanakala, R.; Graeve, O. A. A solvothermal approach for the preparation of nanostructured carbide and boride ultra-high temperature ceramics. *J. Am. Ceram. Soc.* **2010**, *93*, 3035–3038.
- (54) Graeve, O. A.; Madadi, A.; Kanakala, R.; Sinha, K. Analysis of particle and crystallite size in tungsten nanopowder synthesis. *Metall. Mater. Trans. A* **2010**, *41*, 2691–2697.
- (55) Sinha, K.; Kavlicoglu, B.; Liu, Y.; Gordaninejad, F.; Graeve, O. A. A comparative study of thermal behavior of iron and copper nanofluids. *J. Appl. Phys.* **2009**, *106*, 064307.
- (56) Graeve, O. A.; Sinha, K. Dynamic light scattering study of reverse micellar systems for the synthesis of iron-based nanofluids. *Int. J. Mod. Phys. B* **2007**, *21*, 4774–4781.
- (57) Puigdomenech, I. *Hydra-Medusa Software. (Hydrochemical Equilibrium Constant, Database and Make Equilibrium Diagrams Using Sophisticated Algorithms)*. Inorganic Chemistry; Royal Institute of Technology: Stockholm, Sweden, 2004.
- (58) Mathew, M.; Brown, W. E.; Schroeder, L. W.; Dickens, B. Crystal structure of octacalcium bis(hydrogenphosphate) tetrakis(phosphate)pentahydrate, Ca₈(HPO₄)₂(PO₄)·5H₂O. *J. Crystallogr. Spectrosc. Res.* **1988**, *18*, 235–250.
- (59) Sadat-Shojai, M.; Khorasani, M. T.; Jamshidi, A. Hydrothermal processing of hydroxyapatite nanoparticles - A Taguchi experimental design approach. *J. Cryst. Growth* **2012**, *361*, 73–84.
- (60) Díaz de León, J. N.; Picquart, M.; Villarroel, M.; Vrinat, M.; Gil Llambias, F. J.; De los Reyes, J. A. Effect of gallium as an additive in hydrodesulfurization WS_x/-Al₂O₃ catalysts. *J. Mol. Catal. A: Chem.* **2010**, *323*, 1–6.
- (61) Maruyama, T.; Morishima, S.; Bang, H.; Akimoto, K.; Nanishi, Y. Valence transition of Eu ions in GaN near the surface. *J. Cryst. Growth* **2002**, *237*–239, 1167–1171.

- (62) Vercaemst, R.; Poelman, D.; Fiermans, L.; Van Meirhaeghe, R. L.; Lafleure, W. H.; Cardon, F. *J. Electron Spectrosc. Relat. Phenom.* **1995**, *74*, 45–56.
- (63) Yamini, D.; Devanand Venkatasubbu, G.; Kumar, J.; Ramakrishnan, V. Raman scattering studies on PEG functionalized hydroxyapatite nanoparticles. *Spectrochim. Acta, Part A* **2014**, *117*, 299–303.
- (64) Penel, G.; Leroy, G.; Rey, C.; Bres, E. MicroRaman spectral study of the PO_4 and CO_3 vibrational modes in synthetic and biological apatites. *Calcif. Tissue Int.* **1998**, *63*, 475–481.
- (65) Ciobanu, C. S.; Iconaru, S. L.; Massuyeau, F.; Constantin, L. V.; Costescu, A.; Predoi, D. Synthesis, structure, and luminescent properties of europium-doped hydroxyapatite nanocrystalline powders. *J. Nanomater.* **2012**, *2012*, 942801.
- (66) Frumosu, F.; Iconaru, S. L.; Predoi, D. Europium concentration effect of europium doped hydroxyapatite on proliferation of osteoblast cells. *Digest J. Nanomater. Biostructures* **2011**, *6*, 1859–1865.
- (67) De Aza, P. N.; Gutián, F.; Santos, C.; De Aza, S.; Cuscó, R.; Artús, L. Vibrational properties of calcium phosphate compounds. 2. Comparison between hydroxyapatite and β -tricalcium phosphate. *Chem. Mater.* **1997**, *9*, 916–922.
- (68) Koudelka, L.; Mosner, P. Study of the structure and properties of Pb-Zn borophosphate glasses. *J. Non-Cryst. Solids* **2001**, *293*, 635.
- (69) Sinha, K.; Pearson, B.; Casolco, S. R.; Garay, J.; Graeve, O. A. Synthesis and consolidation of $\text{BaAl}_2\text{Si}_2\text{O}_8:\text{Eu}$: Development of an integrated process for luminescent smart ceramic materials. *J. Am. Ceram. Soc.* **2009**, *92*, 2504–2511.
- (70) Zahn, D.; Hochrein, O. On the composition and atomic arrangement of calcium-deficient hydroxyapatite: An ab-initio analysis. *J. Solid State Chem.* **2008**, *181*, 1712–1716.
- (71) Sun, J. P.; Song, Y.; Wen, G. W.; Wang, Y.; Yang, R. Softening of hydroxyapatites by vacancies: A first principle investigation. *Mater. Sci. Eng., C* **2013**, *33*, 1109–1115.
- (72) Zollfrank, C.; Müller, L.; Greil, P.; Müller, F. A. Photoluminescence of annealed biomimetic apatites. *Acta Biomater.* **2005**, *1*, 663–669.